Geraniol and hydrophobic geraniol:thymol eutectic mixtures: Structure and thermophysical characterization

Mohammadreza Haftbaradaran Esfahani [a], Fernando Bergua [a,b], Ignacio Delso [c], Carlos Lafuente [a,b], Manuela Artal [a,b,*]

[a] *Departamento de Química Física, Facultad de Ciencias, Universidad de Zaragoza, Zaragoza, Spain*
[b] *Instituto Agroalimentario de Aragón – IA2 (Universidad de Zaragoza – CITA), Zaragoza, Spain*
[c] *School of Pharmacy, University of East Anglia, Norwich, United Kingdom*

ABSTRACT

The properties of essential oils as food preservatives are well-established. These components have also been used as neoteric solvents to prepare eutectic mixtures. Their high capacity to dissolve poorly water-soluble substances makes them particularly interesting in the biotechnology industry. To implement them, it is essential to determine the structural and chemical-physical properties, as well as develop models to predict the behaviour under any operational condition. Herein, pure geraniol and geraniol/thymol mixtures are studied. Nuclear magnetic resonance experiments and molecular dynamics are used to evaluate the fluid structure. In addition, seven thermophysical properties are measured and correlated. The experimental densities, surface tensions, and viscosities were lower than 952 kg m^{-3}, 33 mN m^{-1}, and 36 mPa s, respectively. These values were adequate for the industrial application of these mixtures. PC-SAFT equation of state well predicted the density with an average deviation of 0.13 %, and the isobaric molar heat capacity with a deviation of 6.9 %. Greater compaction was observed at higher thymol molar ratios and dispersive interactions were predominant. Depending on the composition, geraniol was both an acceptor and donor of hydrogen bonds; conversely, thymol acted as a donor. The article provides the necessary knowledge to be able to use these mixtures and design new ones, as ecological solvents in different applications including those in the agri-food sector.

1. Introduction

The World Health Organization has inferred that around 2.3 billion people in the world (29.3 %) were food insecure in 2021 (The State of Food Security and Nutrition in the World, 2022, 2022). This has increased drastically in vulnerable groups in poor countries. Several foodborne agents, such as bacteria, viruses, parasites, and toxins, are the causative agents. Sulphur derivatives have long been used as synthetic chemicals to eliminate these pathogens; however, they pose a serious threat to consumer health. Therefore, the development of methodologies that include economical and sustainable protective agents is urgently required. The bioactive components of essential oils (EOs) are good candidates for application as natural food preservatives (Perumal et al., 2022). Phenolic compounds exhibit strong antimicrobial and antioxidant activities. Other terpenoids also inhibit the growth of yeast and insects. They also enhance transdermal drug penetration (Schafer et al., 2023). These properties are attributed to the hydrophobicity and

solubility of these substances in the cell membrane. It should be noted that synergetic interactions have been found in mixtures, which are particularly important because they reduce the amount of preservative agent to be used (Chen and Viljoen, 2010; Falleh et al., 2020; Franklin, 2016; Marchese et al., 2016; Perumal et al., 2022). Another application of mixtures of the bioactive components of EOs is their growing application as solvents in the extraction or solubilisation of biomolecules.

The above mixtures usually have a lower melting point than their components and the latter are non-ionic compounds. Therefore, they belong to the Type V deep eutectic solvents (DESs) group although those with ideal behaviour can simply be called eutectic solvents (ESs) (Abranches et al., 2019). All ESs are characterized by containing one or more components that can act as hydrogen bond donors (HBD) and the others as acceptors (HBA) (Tang et al., 2024). Their composition and preparation procedure have significant advantages over other solvents. In addition, they are economical, biodegradable, non-toxic, and do not generate waste. Furthermore, hydrophobic ones are barely soluble in

---

water (Abranches and Coutinho, 2022; Di et al., 2023; Gao et al., 2023; González-Laredo et al., 2023; Li et al., 2023). Because of these characteristics, both DESs and ESs have received considerable attention from the scientific community, particularly in the biotechnology sector. Detailed information on the properties and applications of these neoteric solvents can be found in literature (Abranches and Coutinho, 2022; Boateng, 2023; Castro-Muñoz et al., 2023; Cherniakova et al., 2023; González-Laredo et al., 2023; Marchel et al., 2022; Shamshina and Rogers, 2023; Sportiello et al., 2023). For implementation in different applications, it is necessary to study the interactions between the components and determine their physicochemical properties. Nevertheless, there is a knowledge gap because research has focused on the applications (Marchel et al., 2023). In previous studies, our group has characterised eutectic mixtures containing thymol, menthol, camphor, and carboxylic acids (Bergua et al., 2022a, 2022b, 2021; Hernández-Serrano et al., 2023). In this study, pure geraniol (G) and three of its mixtures with thymol (T) were evaluated.

Geraniol [(2*E*)-3,7-dimethylocta-trans-2,6-dien-1-ol] (G) is a monoterpene alcohol that is insoluble in water and has a characteristic floral flavour and taste. It can be isolated from EOs, such as *palmarosa oil*. According to the U.S. Food and Drug Administration (FDA), G is classified as a "generally recognized as safe" (GRAS) compound and as a substance added to food (synthetic flavouring substance and adjuvants). G is an effective protector against known disease vectors such as mosquitoes and storage food mites. It has been shown to be more effective than traditional synthetic acaricides, with a lower environmental impact (Baker and Grant, 2018). In addition, it has shown anthelminthic activity against several nematodes and marked inhibition of microbial development in animals and humans, even in the gaseous state. Other beneficial effects such as antioxidant, anticancer, and anti-inflammatory activities have also been reported (Baker and Grant, 2018; Chen and Viljoen, 2010). Thymol (5-methyl-2-propan-2-ylphenol) (T) is a phenolic monoterpenoid that is slightly soluble in water and has a pleasant odour. It is the main component of thyme oil and is primarily obtained from *Thymus vulgaris*. A wide variety of beneficial properties of T have been previously reported; it is a potent antioxidant, antiseptic, antibacterial, and antifungal agent. It can also be used as a natural repellent because of its genotoxic effects on insects. Its anaesthetic and healing capacity and anti-inflammatory effects stand out among other biological activities. The European Food Safety Authority (EFSA) classifies T as a safe compound ("Scientific Opinion on the Safety and Efficacy of Phenol Derivatives Containing Ring-Alkyl, Ring-Alkoxy and Side-Chains with an Oxygenated Functional Group (Chemical Group 25). When used as Flavourings for All Species," 2012) and the FDA has approved it as a food additive (synthetic flavouring substance, adjuvants, and preservative in coatings).

Pure G and T, and their eutectic mixtures (GT ESs) are of considerable interest in the agri-food, cosmetic, and pharmaceutical industries (Marchese et al., 2016). Rodriguez-Llorente et al. studied the ability of pure geraniol to separate carboxylic acids and phenolic compounds from wastewater (Gutiérrez-Sánchez et al., 2022; Rodríguez-Llorente et al., 2021, 2019). The high efficiency of astaxanthin extraction from algae has been reported (Pitacco et al., 2022). The application of G, T, and their mixtures as food preservatives is currently under development (Franklin, 2016). However, they have scarcely been characterised in the literature. The density, isobaric molar heat capacity, and vapour pressure of pure G were determined by Martins et al. (2017) and Štejfa et al. (2015). No data on the thermophysical properties of the GT mixtures are available. The results of this work will allow us to expand the database needed for tools such as SUSSOL or PARIS III (Harten et al., 2020; Sels et al., 2020) to provide optimal alternative solvents to conventional ones. This is especially important in applications involving the extraction and processing of components in the food, cosmetics, or pharmaceutical sectors (Bashir et al., 2023; Devi et al., 2023).

The aim of this study was to characterise pure G and binary mixtures of G and T. Several NMR experiments were performed to evaluate the interactions present in the GT ESs. Seven thermophysical properties were evaluated at $p=0.1$ MPa. Other features were calculated and discussed. In addition, the perturbed chain-statistical associating fluid theory (PC-SAFT) equation of state (EoS) was applied to favour the implementation of these solvents in the industry. Finally, the structure of the GT system was also analysed using molecular dynamics.

2. Materials and methods

2.1. Materials

The characteristics and structures of G and T are listed in Table S1. From these compounds, three binary mixtures were prepared in Erlenmeyer flasks by weighing using a PB210S Sartorius balance with an uncertainty of 10^{-4} g. The mixtures were stirred simultaneously and slightly heated (323 K) until a homogeneous liquid was formed. They were then slowly cooled and kept at 298 K until use. The water content determined by the Karl-Fischer method was lower than 300 ppm. The compositions studied were G:T (1:2, molar ratio), G:T (1:1, molar ratio), and G:T (2:1, molar ratio). Hereafter, the acronyms used in this text are GT12, GT11, and GT21. These compositions were chosen because the region close to the equimolar ratio has the widest liquid window, making it the area typically used in applications.

2.2. Nuclear magnetic resonance

NMR experiments were performed using a Bruker NEO spectrometer operating at 400 MHz at ^{1}H and 300 K. The chemical shifts were referenced to tetramethylsilane (TMS), with its chemical shift being considered as 0.0 ppm. The ^{1}H NMR spectra were recorded using a one-pulse sequence with a 30º flip angle (Bruker pulse program *zg30*), with a spectral width of 16 ppm centred at 5 ppm and 16 scans for each spectrum. ^{13}C NMR spectra were obtained using an ATP sequence (Bruker pulse program *jmod*   ) with a spectral width of 190 ppm centred at 90 ppm and 64 scans for each spectrum. Signal assignment was performed using double quantum filtered correlated spectroscopy (DQF-COSY), 1H-13C heteronuclear single quantum coherence (HSQC), and 1H-13C heteronuclear multiple bond correlation (HMBC) (Bruker Pulse Programs *cosygpqf*, *hsqcetgp*, and *hmbcgplpndqf*, respectively). Diffusion experiments were performed using bipolar gradients (Bruker pulse program *ledbpgp2s*). The big and small delta were set to 399.9 and 2.8 ms, respectively. The gradient pulse strength was varied through 25 steps to obtain a 98 % decrease in the resonance intensity. The self-diffusion coefficient, D, was calculated by fitting the intensity of each signal to the following function:

$$I(g) = I_{G=0}\exp\left[-D\gamma_H^2 G^2\delta^2\left(\Delta - \frac{\delta}{3} - \frac{\tau}{2}\right)\right] \tag{1}$$

where $I(g)$ is the measured intensity; $I_{G=0}$ is the intensity in the absence of the gradient; D is the self-diffusion coefficient; γ_H is the gyromagnetic constant of the ^{1}H nucleus; G is the strength gradient; δ is the duration of the bipolar gradient; Δ is the diffusion time; and τ is the time between the end of the gradient and the beginning of the next pulse. Nuclear Overhauser effect spectroscopy (NOESY) experiments were performed using the Bruker pulse program *noesygpph* with a spectral width of 16 ppm centred at 4 ppm and a mixing time, $D8$, of 1 s was used.

2.3. Phase equilibria

The solid-liquid equilibrium (SLE) was determined using a differential scanning calorimeter (TA Instruments DSC Q2000) with an RCS refrigeration system. Standard indium was used to calibrate the temperature and heat flow. The differences between the expected values for indium and those obtained during calibration showed that the uncertainty in T_m was 0.5 K. For each mixture used to generate the SLE dia-

gram, a sample (5–15 mg) was weighed out and placed in an aluminium pan in the liquid state. If the sample was solid at 293 K, the pan was preheated in the DSC at a temperature above the melting point to ensure crystallisation of the mixture inside the device. The samples were first cooled to 213–223 K at a rate of 3 K/min and then heated to 10 K above the melting point at the same scan rate. The reported temperatures corresponded to the maximum peaks owing to the asymmetric peak shapes and the presence of thermal anomalies that hindered the determination of the onset temperature.

2.4. Thermophysical properties

The thermophysical properties were measured using different thermostat apparatus. An Anton Paar DSA 5000 densimeter and sound analyser was used to measure the density (ρ) and speed of sound (u), respectively. The temperature uncertainty was $u(T) = 0.005$ K and the combined expanded uncertainties $U_c(Y)$ (0.95 level of confidence, $k = 2$) of both properties were $U_c(\rho) = 0.05$ kg•m^{-3} and $U_c(u) = 0.5$ m•s^{-1}. A Dr. Kernchen Abbemat-HP refractometer ($u(T) = 0.01$ K) was used to determine the refractive index (n_D) with a $U_c(n_D) = 2 \cdot 10^{-5}$. The isobaric molar heat capacity ($C_{p,m}$) was determined using a TA Instruments Q2000 differential scanning calorimeter. The uncertainties were $u(T) = 0.01$ K and $U_c(C_{p,m}) = 1$ %. The surface tension (γ) was determined using a Lauda TVT-2 drop volume tensiometer. Using this device, $u(T) = 0.01$ K and $U_c(\gamma) = 1$ %. The relative static permittivity (ε_r) was calculated by determining capacitances and resistivities using an Agilent 4263BA LCR high precision impedances analyser connected to an Agilent 16452A cell through four coaxial 16048A cables. Electric fields of 2 MHz and 2 V were applied. The uncertainties were $u(T) = 0.01$ K and $U_c(\varepsilon_r) = 0.02$. Finally, the kinematic viscosity (ν) was measured using different Ubbelohde capillary viscosimeters ($k = 0.02981$ and 0.009434 mm^2•s^{-2}) and a Schoot-Geräte AVS-440 automatic measurement unit. Dynamic viscosity ($\eta = \rho \cdot \nu$) data were calculated from the values of density (ρ) and kinematic viscosity (ν). For this property, $u(T) = 0.01$ K and $U_c(\eta) = 1$ %.

2.5. Molecular dynamics

Molecular dynamics simulations were performed using Assisted Model Building and Energy Refinement software (AMBER18) (Case et al., 2018) and the General Amber Force Field (GAFF) (Wang et al., 2004). The initial cubic simulation boxes were obtained using PackMol software (Martínez et al., 2009). This software randomly packs a given number of each type of molecule into a given volume, minimizing void spaces and intermolecular collisions. In all cases, a cubic simulation box side of 80 Å was used after equilibration. It was previously verified that this box size allowed finding values of constant diffusion coefficients regardless of the chosen molecule. The high number of molecules in each simulation provided sufficient statistical variability. The .*pdb* archives of each compound were generated using the Maestro software (v. 2018–4, NY. USA). Long-range interactions were computed using the Ewald method (Essmann et al., 1995). Van der Waals interactions were described using a Lennard-Jones potential, and a cutoff distance of 10 *Å* was applied. Periodic boundary conditions (PBC) and the leapfrog algorithm (Hockney, 1970) were employed in the simulations. All the simulations were performed in several steps. First, the energy of the system was minimised to avoid the spatial constraints of high energy, which can disrupt the simulation. The system was then gradually heated from 0 to 300 K. Temperature was controlled using Langevin dynamics (Loncharich et al., 1992). This was followed by density equilibration and a final equilibration step, which included monitoring of several structural properties. The last two steps were performed under NPT conditions. For system equilibration, two consecutive productions of 10 ns each were performed. The trajectories were analysed using the VMD (Humphrey et al., 1996) and CPPTRAJ programs (Roe and Cheatham,

2013). Our experimental density values were used to optimize and validate the method.

3. Results and discussion

3.1. NMR studies

NMR is a powerful technique for elucidating the structural aspects of eutectic mixtures because it can provide microscopic information at the molecular level. Hydrophilic eutectic mixtures based on choline chloride were previously characterised by our group using NMR (Delso et al., 2019). In this section, we present a complete study that combines different NMR techniques to shed light on the structural and dynamic features of the three GT ESs.

3.1.1. ^{1}H NMR and ^{13}C NMR experiments

Fig. 1a and b show the ^{1}H NMR and ^{13}C NMR spectra of the eutectic mixtures studied, respectively, and Fig. S1 and S2 (Supplementary File) show the spectra of pure compounds. No overlapping signals or additional peaks are observed in the spectra of the eutectic mixtures. This confirms that no chemical reaction occurs, and no subproducts are generated. The composition of the mixtures was verified by integrating the peaks. GT21 (2:1.00), GT11 (1:1.01), and GT12 (1:2.04), with an uncertainty of $u(x)=0.05$ were determined. It is known that the establishment of interactions causes a change in the chemical shift (δ) of the proton signals by modifying their chemical environment (Gabriele et al., 2019). In our mixtures, the variation of δ with the composition is considerably small, suggesting the presence of weak interactions (Posada et al., 2019). This slight change is different for the T and G signals, which suggests that the dispersive interactions in the T and G molecules are different, likely because of the presence of microheterogeneities (Malik and Kashyap, 2021). Generally, a unique signal is obtained for all mobile protons in a sample owing to chemical exchange (Charisiadis et al., 2014; Duarte et al., 2017). Nevertheless, the signals of the mobile protons appear as separated peaks in the GT ESs. They present the highest change in δ. This behaviour implies slow exchange as a consequence of the formation of hydrogen bonds (HB) with a long lifetime. Furthermore, a trend is observed with the composition; the δ of the mobile proton of T (OH-T) increases with x_G and that of G (OH-G) decreases with x_T. The trend of T acting as an HBD, owing to the resonance effect of its aromatic ring, (Abranches et al., 2019) is greater at higher G compositions. Consequently, the OH-T environment is less shielded, and the signal shifts to a higher ppm. However, the greater is the value of x_T, the greater is the probability of G to act as an HBA. Subsequently, the electronic density increases, and OH-G is shielded.

3.1.2. NOESY experiments

The nuclear Overhauser effect (NOE) occurs when a perturbed spin induces a change in the spin population of a nearby nucleus. Thus, these spectra provide information on the three-dimensional molecular geometry, revealing the proximity of protons to each other. Negative nOes are related to large and slow-moving molecules, and positive nOes are indicative of small and dynamic molecules with high rotation rates. (Claridge, 2016) Negative nOes have been observed in DESs with supramolecular structure (Delso et al., 2019). Fig. 2 shows the NOESY spectra of the GT mixtures. All the crosspeaks in the NOESY spectra appeared as positive, as opposed to the diagonal negative signals, except two of them, suggesting the formation of a weak intermolecular network. Apart from the expected negative crosspeak due to chemical exchange between the two hydroxyl groups, one more negative crosspeak was observed. This crosspeak, correlating the hydroxyl mobile proton in T with adjacent protons to the OH of geraniol (named "g") can be due to transferred NOE from the OH exchange peak. The rest of signals were due to intramolecular or intracomponent contacts. Interestingly, GT21 mixture exhibited NOE signal between proton "5" of T and proton "g" of G that disappeared at x_T increasing. This fact suggests
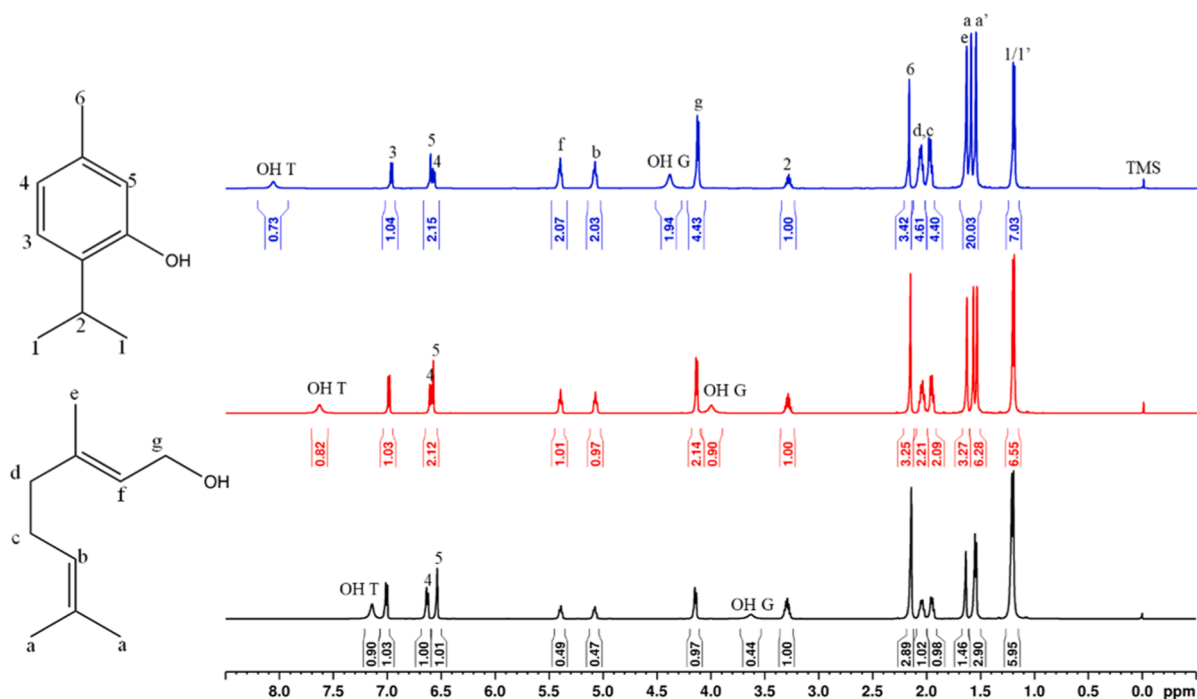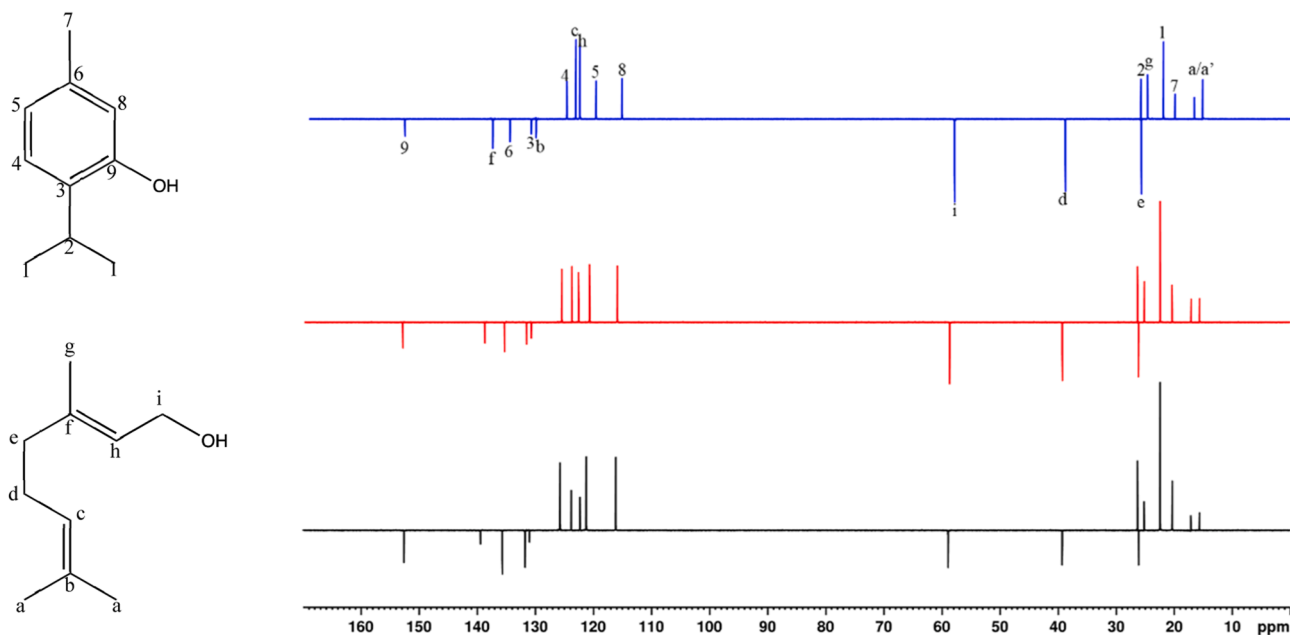
Fig. 1. Spectra of GT eutectic mixtures; (-) GT21, (-) GT11 y (-) GT12. (a) ^{1}H NMR; (b) ^{13}C NMR.

that this intercomponent HB is predominant at G-rich compositions.

3.1.3. DOSY experiments

This technique provides information on translational diffusion owing to the Brownian motion of molecules through the self-diffusion coefficient D. This parameter depends on the size and form of the molecule, temperature, and solvent viscosity. Hence, phenomena such as aggregation and formation of strong interactions significantly influence D. Thus, this technique is a powerful tool for studying the interactions between different species in a mixture as well as their dynamic characteristics. As the molecules are indistinguishable in this experiment, the value of D represents the average molecular motion of all molecules. Table 1 lists the D values of the mobile and aliphatic protons of the pure compounds and the studied mixtures. These values are within the ranges reported for other eutectic solvents (Duarte et al., 2017). The spectra of the three mixtures are similar, and those of GT12 are shown in Fig. S4. For all compositions, the mobile G and T protons diffuse similarly and are faster than the aliphatic protons. The D values of T are higher than those of G for all the compositions, and the greatest difference is observed in the T-rich composition. In this case, the G molecules tend to act as HBAs and the remaining T molecules do not interact in more dynamic environments.
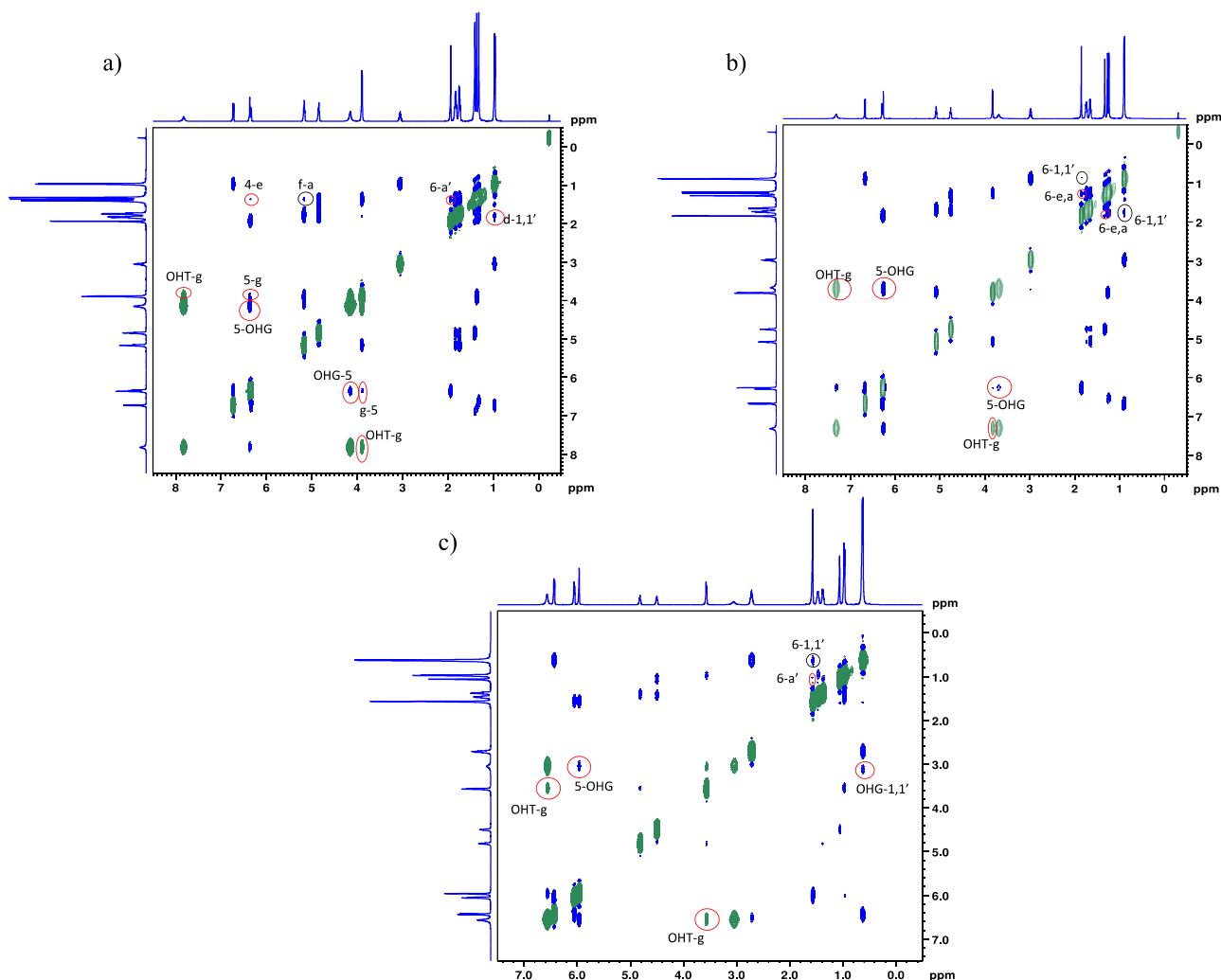
Fig. 2. NOESY spectra of GT mixtures: a) GT21, b) GT11 and c) GT12; (■) positive signal; (■) negative signal; (O) intramolecular interactions; (⭕) intermolecular interactions. Only the more relevant crosspeaks are assigned, for a full peak assignment see Fig S3.

Table 1
Self-diffusion coefficients, *D*, of mobile and aliphatic protons of each compound at 300 K obtained by PFG NMR and MD.

|	Proton type	$10^{11}D_{NMR}(G)/$ m²•s⁻¹	$10^{11}D_{MD}(G)/$ m²•s⁻¹	$10^{11}D_{NMR}(T)/$ m²•s⁻¹	$10^{11}D_{MD}(T)/$ m²•s⁻¹
G	Mobile	13.50			
	Aliphatic	12.89			
GT21	Mobile	12.12		12.12	
	Aliphatic	11.54	8.7	12.21	8.22
GT11	Mobile	11.72		11.66	
	Aliphatic	10.65	7.13	12.00	6.90
GT12	Mobile	9.804		9.798	
	Aliphatic	8.51	5.36	10.21	5.03
T diluted in CDCl₃	Mobile			17.69	
	Aliphatic			17.64	

3.2. SLE

In the design and characterisation of eutectic mixtures, the measurement of the solid-liquid phase diagram is necessary. However, we found serious problems in determining the melting temperatures (T_m) of the mixtures included in this study. This was a consequence of the remarkably low melting point of G. The value determined experimentally by Štejfa et al. (2015) is T_m=183 K, making it difficult to crystallise the GT ESs. Thus, we only obtained results for the two T-rich compositions. The values were $T_m = 312.48$ K for $x_T = 0.75$ and $T_m = 312.97$ K

for $x_T = 0.85$; Fig. S5 shows the obtained thermograms.

3.3. Thermophysical properties

Thermophysical properties including the density (ρ), speed of sound (u), refractive index (n_D), static permittivity (ε_r), isobaric molar heat capacity ($C_{p,m}$), surface tension (γ), and dynamic viscosity (η) were investigated. They were determined at $p =0.1$ MPa and at temperatures ranging from 278.15 to 338.15 K. All experimental data are listed in Table S2 and are shown in Fig. 3 and S6. Moreover, the values for each
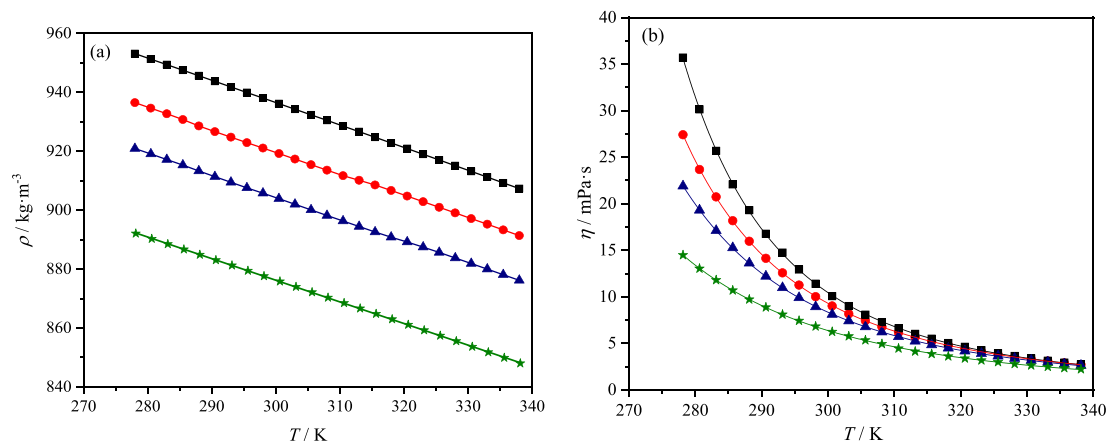
Fig. 3. Experimental thermophysical properties of G and GT ESs at $p = 0.1$ MPa and at various temperatures and compositions. (a) density, ρ; (b) dynamic viscosity, η. (★) pure G; (▲), GT21; (●) GT11; (■) GT12. Points, experimental values; lines, correlated data.

property at the two T (298.15 K and 313.15 K) are summarised in Table 2 for easier follow-up of the discussion. The properties are correlated with T and the equations and coefficients are listed in Table 3.

3.3.1. Density

The ρ value of the pure G ranged from 847.98 to 892.07 kg·m^{-3} and those of the GT mixtures were contained within 876.16 and 953.12 kg·m^{-3}. Thus, all liquids had lower density than water, and the difference was higher than 6 %. Consequently, they can be employed in phase separation processes (Jones and Harris, 1992; Rodríguez-Llorente et al., 2020). Martins et al. (Martins et al., 2017) calculated the density of pure G in the T range of 278.15–368.15 K and $p = 0.1$ MPa. By comparing with our data, the mean relative deviation was $MRD(\rho)$=1.07 %. In addition, the National Toxicology Program (Program, n.d.) and Larrañaga et al. (Larrañaga et al., 2016) reported the ρ value at 293.15 K, and the deviations calculated were 0.92 % and 0.55 %, respectively. However, there is no ρ data for the GT mixtures. The ρ increased with the molar fraction of thymol (x_T). The flat shape of the aromatic ring favoured the compaction of the mixtures. Fig. 3a shows the effect of T on ρ. The density decreases with increasing T because of the increased thermal motion. To quantify the effect of T on ρ, the isobaric thermal expansion coefficient (α_p) was calculated as follows:

$$\alpha_p = -\frac{1}{\rho}\left(\frac{\partial\rho}{\partial T}\right)_p \tag{2}$$

Where ρ, T and p are the density, temperature and pressure, respectively. This property is a basic parameter in the design of industrial operations because T fluctuations are common in facilities and can be decisive in processes. The differences of α_p values of the GT mixtures were within

Table 2
Summary of the thermophysical properties of the liquids studied at $p = 0.1$ MPa.

Property	T/ K	GT12	GT11	GT21	G
ρ / kg• m^{-3}	298.15	938.02	921.04	905.74	877.60
	313.15	926.62	910.13	894.42	866.63
u / m•s^{-1}	298.15	1422.21	1421.96	1415.29	1413.78
	313.15	1371.74	1370.98	1359.16	1360.79
$C_{p,m}$ / J•mol^{-1}•K^{-1}	298.15	354	344	361	376
	313.15	364	356	375	392
n_D	298.15	1.50544	1.49771	1.49017	1.47494
	313.15	1.49876	1.49112	1.48370	1.46868
ε_r	298.15	5.824	6.465	6.931	7.827
	313.15	5.595	6.162	6.558	7.086
γ /mN•m^{-1}	298.15	31.12	30.73	30.49	29.94
	313.15	29.99	29.66	29.26	28.86
η /mPa•s	298.15	11.395	10.002	8.919	6.819
	313.15	6.005	5.632	5.233	4.117

Table 3
Fitting parameters (A_Y, B_Y, C_Y) and regression coefficients, R^2, for the thermophysical properties of the investigated liquids.

Property	GT ESs	A_Y	B_Y	C_Y	R^2
ρ[a] / kg•m^{-3}	GT12	1165.41	−0.7632		0.99997
	GT11	1143.02	−0.7442		0.99973
	GT21	1127.05	−0.7424		0.99984
	G	1096.41	−0.7341		0.99996
u[a] / m•s^{-1}	GT12	2422.82	−3.3558		0.99989
	GT11	2439.78	−3.4134		0.99986
	GT21	2513.22	−3.6830		0.99976
	G	2460.36	−3.5075		0.99968
$C_{p,m}$ / J•mol^{-1}•K^{-1}	GT12	152.28	0.67446		0.99876
	GT11	114.67	0.76862		0.99912
	GT21	100.89	0.87292		0.99945
	G	60.33	1.05815		0.99950
n_D[a]	GT12	1.63822	−4.45•10^{-4}		1.00000
	GT11	1.62837	−4.38•10^{-4}		0.99995
	GT21	1.61940	−4.34•10^{-4}		0.99994
	G	1.60180	−4.25•10^{-4}		0.99721
ε_r[b]	GT12	6.284	0.0118	−4.48•10^{-5}	0.99986
	GT11	14.728	−0.0346	2.31•10^{-5}	0.99999
	GT21	17.735	−0.0467	3.52•10^{-5}	0.99984
	G	40.954	−0.1726	2.06•10^{-4}	0.99772
γ[a] / mN•m^{-1}	GT12	54.44	−0.0782		0.99964
	GT11	53.58	−0.0764		0.99963
	GT21	53.55	−0.0775		0.99954
	G	51.04	−0.0708		0.99989
η[c] / mPa s	GT12	0.03273	718.25	175.44	0.99995
	GT11	0.03140	779.16	163.09	0.99998
	GT21	0.02120	938.56	142.93	0.99999
	G	0.00699	1385.62	96.70	0.99990

[a] $Y = A_Y + B_Y T$; [b] $Y = A_Y + B_Y T + C_Y T^2$; [c] $Y = A_Y \exp[\frac{B_Y}{T - C_Y}]$.

the calculated uncertainty, which showed that the effect of T on ρ was similar for all of them (Table S3). In this way, a single value of $\alpha_p = 0.821$ ($\pm$ 0.04) k•K^{-1} could be obtained. The lower density and lower compactness of pure G versus GT mixtures yielded higher α_p values. For this compound, the average value was $\alpha_p = 0.844$ ($\pm$ 0.04) k•K^{-1}. The α_p increased with increasing T (Fig. S7a).

Predicting the behaviour of fluids at any pressure, temperature, or composition is a useful tool in process design. For this purpose, easy-to-apply thermodynamic models, such as EoSs, are preferred. In this study, we validated the PC-SAFT EoS (Gross and Sadowski, 2001, 2000) for the pure G and GT ESs. A brief summary of the model and the values of all the parameters are provided in Table S4. We used the commercial VLXE software to perform the calculations (Laursen, 2012). As an open-source

toolkit, Clapeyron.jl (Walker et al., 2022) allows to obtain thermodynamic properties using various EoS and models, including PC-SAFT. The parameters of pure T were obtained from literature (Martins et al., 2018). The PC-SAFT parameters of pure G were estimated by fitting the vapour pressures obtained from the literature (Linstrom and Mallard, 2020; Štejfa et al., 2015) and our density data. The averages of the deviations were Δp_v = 5.6 Pa and $MRD(\rho)$=0.03 %; a graphical display is shown in Fig. S8. For the mixtures, the predictive version of the model was used. Therefore, the binary interaction parameter was null (k_{ij}). The model accurately predicted the densities of the mixtures. The average of the deviations obtained was $MRD(\rho)$=0.13 % and were greater at higher x_T and T (Fig. S9a). A slight decrease in this average deviation can be obtained by introducing an optimized binary interaction parameter. Thus, $MRD(\rho)$=0.09 with k_{ij}=–0.008. However, we do not believe that this decrease justifies its inclusion in the model.

3.3.2. Speed of sound

The u values at each T were very similar for all the investigated fluids. They ranged from 1276.41 m•s^{-1} of pure G at 338.15 K to 1492.20 m•s^{-1} of GT11 at 278.15 K. This property is related to the compaction of the fluid. Therefore, the higher the value of T, the lower the value of u (Fig. S6a). In addition, the isentropic compressibility (κ_s) and intermolecular free length (L_f) can be calculated as follows:

$$\kappa_s = \frac{1}{\rho u^2} \qquad (3)$$

$$L_f = K\sqrt{\kappa_s} \qquad (4)$$

Where ρ and u are the density and the speed of sound at similar temperature and pressure, and K is the Jacobson's constant (Jacobson, 2004). The values of κ_s and L_f (Table S3) ranged from 471.85 to 723.83 ($\pm$ 0.25) TPa^{-1}, and 0.414–0.570 ($\pm$ 0.005) Å, respectively. The GT12 mixture at 278.15 K presented the lowest data, and the pure G at 338.15 K exhibited the highest. Both properties increased with T and x_G (Fig. S7b) because of the decrease in compactness due to thermal motion. It is known that the EoS does not adequately represent this property. The average deviation obtained between our measurements and the u predicted with PC-SAFT EoS was 17 %. It decreased with increasing T and no trend was observed with the composition (Fig. S9b). The deviation increased slightly ($MRD(u)$=17.4) with the optimized parameter (k_{ij}=–0.008).

3.3.3. Isobaric molar heat capacity

The $C_{p,m}$ of the investigated solvents were within the range of 328 and 417 J•mol^{-1}•K^{-1} and increased with T owing to the higher energy for storage (Fig. S6b). The $C_{p,m}$ data of pure G reported by Štejfa et al. (Štejfa et al., 2015) were a 9 % lower than ours. The deviation of $MRD(C_{p,m})$= 8.3 % can be attributed to the use of a higher heating rate in the DSC experiment. In the model with PC-SAFT EoS, the mean relative deviation with respect to the predicted data was 6.90 % and increased with T (Fig. S9c). The deviation hardly changed ($MRD(C_{p,m})$=7.0) when introducing the optimized parameter (k_{ij}=–0.008).

3.3.4. Refractive index

The n_D evaluates the compactness of fluids; thus, a less compact structure of a fluid has a lower n_D value. This property yielded results similar to those previously reported, in which the GT12 mixture exhibited the greatest compaction. The aromatic ring of T favoured the packing of the fluid. In contrast, thermal agitation hindered this process (Fig. S6c). The molar refraction (R_m) is related to the volume occupied by a mole of molecules and is calculated as follows:

$$R_m = V_m \frac{(n_D^2 - 1)}{(n_D^2 + 2)} \qquad (5)$$

Where n_D is the refractive index and V_m is the molar volume. An estimation of the free volume (f_m) in the fluid can be performed by subtracting R_m from V_m. The R_m and f_m (Table S3 and Fig. S7c) increased with T and the change was most pronounced in f_m. The ratio of these parameters is the percentage of free volume; the values ranged from 69.9 % for GT12 at 278.15 K to 72.7 % for pure G at 338.15 K.

3.3.5. Static permittivity

The ε_r facilitates the estimation of the polarity of non-ionic fluids. Table S2 lists the experimental data and Fig. S6d shows the effect of T on this property. The higher the x_G, the greater the ε_r value and effect of T. By combining the above data at similar p and T conditions, an estimation of the orientation of dipoles can be performed using the following Fröhlich equation (Fröhlich, 1948):

$$g\mu^2 = \frac{9kT\varepsilon_0 V_m}{N_A} \frac{(\varepsilon_r - n_D^2)(2\varepsilon_r + n_D^2)}{\varepsilon_r(n_D^2 + 2)^2} \qquad (6)$$

where k is the Boltzmann constant, N_A is the Avogadro number, T is the temperature in Kelvin, ε_0 is the static permittivity at vacuum, μ is the dipole moment, n_D is the refractive index, V_m is the molar volume, and g is the Kirkwood–Fröhlich correlation parameter. This parameter was higher in pure G and decreased significantly with increasing x_T (Table S3). In contrast with the other solvents studied, GT12 and GT11 exhibited a slight increase of $g\mu^2$ with T (Fig. S7d). This behaviour was also opposite to that observed for ε_r. An increase in thermal agitation can destabilise the cyclic aggregates, thereby increasing the number of aggregates with a linear chain configuration. In addition, the g factor serves as an indicator of the relative alignment of adjacent dipoles within a liquid. For dipoles with a parallel preferential arrangement, g >1. In contrast, for a fluid featuring antiparallel dipoles, g <1. It can be calculated by estimating μ^2 as the sum of contributions of the pure components of the mixture ($\mu^2 = x_1\mu_1^2 + x_2\mu_2^2$). Table S1 lists the μ_i values of our pure compounds. For pure G, g ranges from 1.39 to 1.61 and is within 1.21–1.44 for GT ESs. The results indicate that a parallel orientation of the dipoles is preferred, which is favoured by the presence of G.

3.3.6. Surface tension

The γ is related to the characteristics of the liquid-air interface. This knowledge is essential, particularly for applications that require fluid atomisation. Low γ values enhance the efficiency of solvent atomisation processes. The measured γ ranged from 27.10 to 32.65 mN•m^{-1}. The higher the x_T, the higher the γ values. This was in agreement with the fact that the mixture with maximum T content was the most structured and compact. This sequence was also consistent with γ of pure T (Jasper, 1972). The structuring of the fluid became more difficult as T increased; therefore, the values decreased as the temperature increased (Fig. S6e). The effect of T on γ provides information regarding the energy necessary to display a number of molecules towards the air-liquid interface. The entropy of surface (ΔS_S) and the enthalpy of surface (ΔH_S) were calculated as follows:

$$\Delta S_s = - \left(\frac{\partial \gamma}{\partial T} \right)_p \qquad (7)$$

$$\Delta H_S = \gamma - T \left(\frac{\partial \gamma}{\partial T} \right)_p \qquad (8)$$

Where γ, T and p are the surface tension, temperature and pressure, respectively. Both properties were almost similar at all x_T and T and the average values were: 0.077 $\pm$ 0.001 mN•m^{-1}•K^{-1} and 53.9 $\pm$ 0.4 mN•m^{-1}, respectively. Several correlations to estimate the critical temperature (T_c) from the experimental γ data have been proposed (Cotterman and Prausnitz, 1986). This property is essential for thermodynamic modelling; however, its measurement is usually difficult or

impossible. Herein, we used the Guggenheim equation (Guggenheim, 2004) based on the theory of corresponding states, which is expressed as

$$\gamma = \gamma_0 \left(1 - \frac{T}{T_c}\right)^{\frac{11}{9}} \tag{9}$$

Where γ_0 is a constant, T is the temperature, and T_c is the critical temperature. For our solvents, $\gamma_0 = 59$ mN·m^{-1}. In addition, we used the PC-SAFT EoS to predict the critical locus of the GT system. Table S5 lists the values obtained using Eq. (9), the thermodynamic model, and pure compounds reported in the literature. Comparing the first two, the deviation in T_c is less than 10 %.

3.3.7. Viscosity

The fluidity of a mixture plays a crucial role in the design and optimisation of industrial processes and is influenced by factors such as the molecular size, shape, and intermolecular interactions (Abbott et al., 2011, 2007; D'Agostino et al., 2011; Dai et al., 2015). In general, a high η value of a solvent is a major drawback for its industrial use. Van Osch et al. (Van Osch et al., 2019) proposed a value of 100 mPa·s as the upper limit to ensure an optimal performance in engineering processes. This property is the main problem of the hydrophilic eutectics for which values of up to $5.1 \bullet 10^5$ mPa·s at 313.15 K have been reported (Aroso et al., 2017). In our mixtures, η was within 2.614–35.687 mPa·s for GT ESs and 2.213–14.474 mPa·s for G. Considering this property, they could be suitable solvents in this T range (278–338 K). The higher the x_T, the more viscous the fluid. This may be related to the higher number of interactions in the most T-rich mixture. As expected, the trend of η with x_T was opposite to that obtained for the D coefficient because fluidity and diffusivity were inversely proportional. The effect of T on transport properties as η is particularly marked at low T following the η and T relationship an exponential equation (Fig. 3b). The VFT correlation used is as follows:

$$\eta = A_Y \exp\left(\frac{B_Y}{T - C_Y}\right) \tag{10}$$

Where T (in K) is the temperature, and A_Y, B_Y, and C_Y are the fitting parameters (Table 3). A_Y represents the η at $T \rightarrow \infty$. At this T, η is only due to steric constraints. B_Y, and C_Y facilitate the calculation of the energetic barrier of a molecule for moving between the layers of the fluid; that is, the activation energy for viscous flow ($E_{a,\eta}$), which is calculated as follows:

$$E_{a,\eta} = R\frac{\partial(\ln\eta)}{\partial\left(\frac{1}{T}\right)} = R\left(\frac{B_Y}{\left(\frac{C_Y^2}{T^2} - \frac{2C_Y}{T} + 1\right)}\right) \tag{11}$$

Where T (in K) is the temperature, and B_Y, and C_Y are the above fitting parameters. The $E_{a,\eta}$ values are listed in Table S3 and Fig. S7e. At 298.15 K, $E_{a,\eta}$ is 25.2 kJ·mol^{-1} for G and varies from 28.8 to 34.4 kJ·mol^{-1} for GT ESs. The larger shape and size of the G molecules compared with those of the T molecules generate greater steric hindrance, as shown by the increase in A_Y with x_G. However, the increase of the interactions with x_T in turn implies higher $E_{a,\eta}$. Correlations between η and γ data at similar conditions has been reported. The Pelofsky and Murkerjee equations (Ghaedi et al., 2017; Pelofsky, 1966) previously validated for various types of fluids were used. The expressions and corresponding fit coefficients are listed in Table S6. Adequate agreement between the experimental and fitted data is observed, as indicated by the high linearity (R^2>0.97).

3.4. Molecular dynamics

Molecular dynamics simulations have emerged as the predominant computational technique for investigating the nanostructures and dynamic behaviours of ESs. This helps elucidate the molecular nature of the mixtures, providing insights into the interactions between the compounds at the atomic level. In this section, we describe the structure of the GT ESs by calculating the diffusion coefficients (D), radial distribution function (RDF), number of HBs (N_{HB}), and noncovalent interaction (NCI) index. First, the box dimensions and number of molecules was optimised. Density was used as a parameter to verify the model used for comparison with our experimental data. The results are listed in Table S7, and the average deviation is less than 2.5 %. This value confirms that the chosen force field (GAFF) and simulation boxes are appropriate for these systems (Fan et al., 2021b, 2021a).

3.4.1. Self-diffusion coefficients

The D values were calculated using the following Einstein relation:

$$D = \frac{1}{2n}\lim_{t \to \infty}\frac{d}{dt}\left\langle |r_i(t) - r_i(0)|^2 \right\rangle \tag{12}$$

Where n is the number of systems (three in this case), t is the simulation time, $r_i(t)$ is the position of the molecule at time t, and $r_i(0)$ is the position at the beginning of production. The value of $\left\langle |r_i(t) - r_i(0)|^2 \right\rangle$ is the mean-square displacement (MSD) of each molecule. It is important to note that the calculation of D must be performed under diffusion regime conditions, which are reached when the variation in MSD with time is linear (Méndez-Morales et al., 2013; Wu et al., 2016). Figure S10 shows the regression lines of MSD obtained from the raw data obtained using AMBER.

The D coefficients were calculated as one-sixth of the slope and the values are reported in Table 1. Calculated D values showed a good correlation with those measured experimentally, reproducing the decrease of the viscosity of mixtures as x_G decreased. Contrary to what was obtained in Section 3.1.3., G showed slightly higher values than T, differences within reason frequently attributed to the force field (GAFF) used (Velez and Acevedo, 2022).

3.4.2. Radial distribution function

The RDFs were calculated using the VMD software for pairs of atoms that were liable to form HBs. That is, the oxygen of the hydroxyl group (O1 of T and G) acted as the HBA, and the hydrogen of the same group (H14 of T and H18 of G) acted as the HBD. Atom labelling is shown in Fig. S11 and Fig. S12 presents the RDFs of each mixture for the studied atomic pairs. The RDF is expressed as $g(r)$, which represents the probability that an atom is localised at a distance r from another atom. All functions show a maximum peak at approximately 2 Å. These distances are related to intermolecular hydrogen bonding and our values agree with those reported by Panda and Bhargava (2022) for similar mixtures. In addition, the higher the peak height, the more significant the interaction. G has been reported to be a strong HBA and T is known to be a strong HBD owing to the resonance effect of its aromatic ring (Abranches and Coutinho, 2022; Fan et al., 2021b). As expected, the most significant interaction was GO1-TH7, in which G acted as the HBA and T as the HBD. This interaction was the most probable at equimolar composition, followed closely by a T-rich composition. It was deduced that the interaction GO1-GH18 stood out in all mixtures, being the second most important. This suggested that G might act as an HBD, as observed for menthol in its mixture with T (Schaeffer et al., 2021). In contrast, T acting as an HBA and T or G acting as an HBD were the two least probable interactions. The fact of a phenolic alcohol being an excellent HBD and a very poor HBA was already reported for naphtol (Panda and Bhargava, 2022). A second group of small peaks were observed at distances around 3.5 Å, corresponding to the pair of O and H not directly involved in the HB. The presence of only these two peaks confirms the formation of pairs of molecules, where each molecule only establishes a HB with one other molecule.

3.4.3. Number of hydrogen bonds

This section presents a quantitative evaluation of the significance of these interactions. The criteria used for N_{HB} calculations were those published by van der Spoel et al. (van der Spoel et al., 2006) and Luzar et al. (Luzar and Chandler, 1993). The results are listed in Table S8 and shown in Fig. 4. These are expressed as the ratio of the number of HBs of a specific type to the total number of molecules in the system involved in that type of bond. The increase in the total number of HBs with x_G is due to the significant increase in the number of GO1-GH18 HBs. Conversely, the inter-component interactions remain almost constant. The maximum ratio of 0.5 HB per molecule is in fully agreement with the above discussed RDF result, that confirm the formation of molecular pairs.

3.4.4. Non-covalent interactions

An overall view of the interaction of molecules is provided by calculating the NCI index (Johnson et al., 2010). The equimolar mixture was chosen because the results are similar for all compositions. This index enables the identification and analysis of NCI (hydrogen bonds, dipole-dipole interactions, London dispersion forces, and steric repulsions) based on the molecular geometry of the mixture. This tool uses electron density (ρ) and its derivative, the reduced density gradient (RDG or s), to visualise NCI as surfaces within the real space of the sample. The value of the reduced gradient is close to zero in regions with covalent and non-covalent bonds and downward-pointing peaks appear in the RDG versus ρ plot. Regions of low ρ are associated with weak interactions such as van der Waals forces, whereas regions of high ρ (positive or negative) are related to stronger interactions. To distinguish them, the sign of the second Hessian eigenvalue of the density (λ_2) is used. Therefore, attractive and repulsive interactions are identified in regions where $\lambda_2 < 0$ and $\lambda_2 > 0$, respectively, whereas van der Waals interactions have $\lambda_2 \approx 0$. In this way, RDG is represented against the $\lambda_2 \bullet \rho$ product and the colour code is shown in Fig. 5.

It was observed the establishment of only one HB and the presence of large isosurfaces of hydrophobic van der Waals interactions. HBs are surrounded by different van der Waals interactions, which stabilise them. Therefore, the polar and nonpolar regions are arranged, causing structural heterogeneity in the system (Fan et al., 2021b). The observed van der Waals interactions correspond to π-π interactions both between the aromatic rings of T and the aromatic ring of T and olefinic protons of G, CH-π interactions both between T molecules and the G and T ones, and aliphatic interactions between the methyl groups of T and G. The repulsive interactions are related to the constraints of the aromatic ring

of T. The amount and size of these isosurfaces due to van der Waals interactions could justify the importance of the hydrophobic interactions, along with the HB, for the formation of the eutectic phase (Gutiérrez et al., 2020).

These findings are in good agreement with the detection in the NOESY experiments of crosspeaks correlating hydrogens in proximity to the hydroxyl groups (Fig. 2), demonstrating not only the spatial proximity of these pairs of protons, but suggesting the higher stability of the hydrogen bonds. Longer half-lives are required to allow the NOE effect to build up, that can be observed between hydrogens 5 in T and g in G. On the other hand, crosspeaks observed among methyl groups (e, a, and a' in G; and 6, 1, and 1' in T), both intermolecular and intracomponent (distant more than 5 Å) strongly support the importance of the hydrophobic and van der Waals forces in the intermolecular interactions.

4. Conclusion

A comprehensive thermophysical and structural characterisation of hydrophobic eutectic mixtures based on thymol and geraniol in molar ratios of 2:1, 1:1, and 1:2 was conducted. This thermophysical study focused on density, speed of sound, refractive index, static permittivity, isobaric molar heat capacity, surface tension, and dynamic viscosity. Additionally, derived properties such as isobaric thermal expansibility, isentropic compressibility, intermolecular free length, molar refraction, free volume, entropy, enthalpy surface, critical temperature, and flow viscosity energy were obtained. NMR experiments and molecular dynamics calculations were performed to analyse the structure and obtain auto-diffusion coefficients. The results can be used in the search for sustainable solvents and their subsequent implementation in the design of industrial processes.

Thermophysical characterisation revealed that the densities of pure G and GT ESs were lower than those of water at the same temperature, indicating favourable phase separation during the extraction processes in aqueous media. In addition, the mixtures became less compact as the molar fraction of G increased. The heat capacities of G were slightly higher than those of the other mixtures. The surface tensions and viscosities were moderate making the mixtures suitable for industrial applications. Structural characterisation revealed the absence of strong supramolecular structures. These results agreed with the obtained values of the thermophysical properties, such as low viscosity. The NCI and NOESY experiments showed that the main interactions established were dispersive, exhibiting π-π interactions and aliphatic interactions between the methyl groups of T and G. In the dominant hydrogen bond, G acted as the HBA and T as the HBD, followed by the formation of a HB between the G molecules. In this system, T tended to act as an HBD and G could act as an HBA or HBD, depending on the composition of the mixture. The distribution of HB varied with the composition. Nevertheless, on average, the structure of the mixture remained similar across all compositions owing to its reliance on dispersive interactions.

CRediT authorship contribution statement

Manuela Artal: Writing – review & editing, Writing – original draft, Project administration. **Mohammadreza Haftbaradaran Esfahani:** Resources, Investigation, Data curation. **Ignacio Delso:** Formal analysis. **Fernando Bergua:** Writing – review & editing, Formal analysis, Data curation. **Carlos Lafuente:** Writing – original draft, Validation.

Declaration of Competing Interest

The authors declare that they have no known competing financial interests or personal relationships that could have appeared to influence the work reported in this paper.
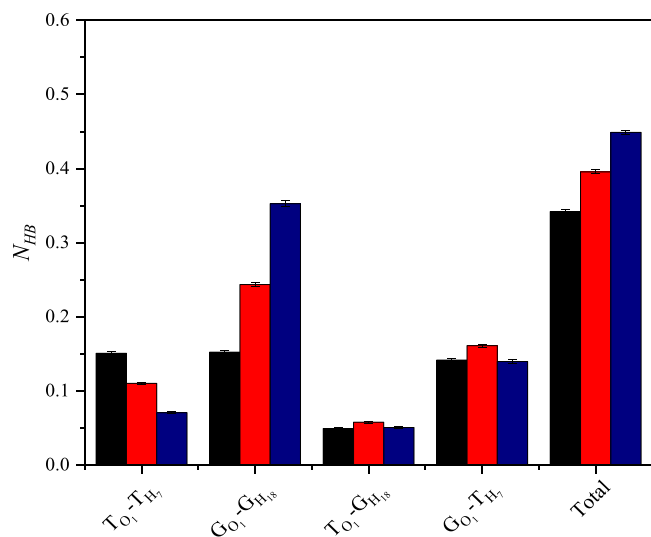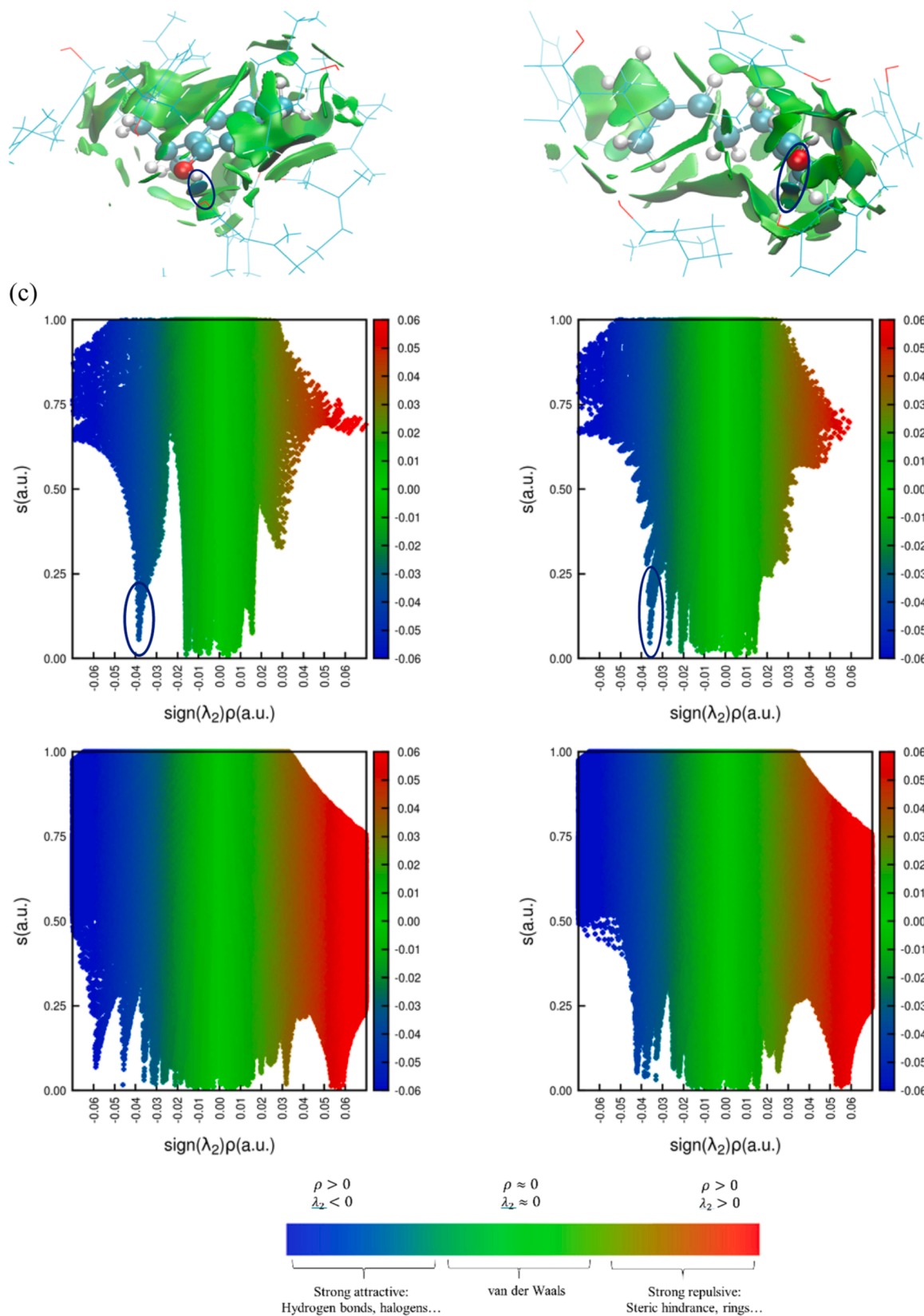

Fig. 4. Ratio between the number of HBs and number of molecules involved in this type of bond in the GT system; (■) GT21, (■) GT11 y (■) GT12.

Fig. 5. Three-dimensional visualization of RDG and representation of RDG versus $(\lambda_2)\rho$ of (a) T and (b) G in GT11 random frame and c) representation of RDG versus $(\lambda_2)\rho$ in GT11 mixture.

Data availability

All data used in the research are found in the main text or the supplementary file

Acknowledgements

Appendix A. Supporting information

Supplementary data associated with this article can be found in the online version at doi:10.1016/j.indcrop.2024.119781.

References

Abbott, A.P., Harris, R.C., Ryder, K.S., 2007. Application of hole theory to define ionic liquids by their transport properties. J. Phys. Chem. B 111, 4910–4913. https://doi.org/10.1021/jp0671998.

Abbott, A.P., Harris, R.C., Ryder, K.S., D'Agostino, C., Gladden, L.F., Mantle, M.D., 2011. Glycerol eutectics as sustainable solvent systems. Green Chem. 13, 82–90. https://doi.org/10.1039/C0GC00395F.

Abranches, D.O., Coutinho, J.A.P., 2022. Type V deep eutectic solvents: design and applications. Curr. Opin. Green Sustain Chem. 35, 100612. https://doi.org/10.1016/j.cogsc.2022.100612.

Abranches, D.O., Martins, M.A.R., Silva, L.P., Schaeffer, N., Pinho, S.P., Coutinho, J.A.P., 2019. Phenolic hydrogen bond donors in the formation of non-ionic deep eutectic solvents: the quest for type v des. Chem. Commun. 55, 10253–10256. https://doi.org/10.1039/c9cc04846d.

Aroso, I.M., Paiva, A., Reis, R.L., Duarte, A.R.C., 2017. Natural deep eutectic solvents from choline chloride and betaine – physicochemical properties. J. Mol. Liq. 241, 654–661. https://doi.org/10.1016/j.molliq.2017.06.051.

Baker, B.P., Grant, J.A., 2018. Geraniol Profile Active Ingredient Eligible for Minimum Risk Pesticide Use.

Bashir, I., Dar, A.H., Dash, K.K., Pandey, V.K., Fayaz, U., Shams, R., Srivastava, S., Singh, R., 2023. Deep eutectic solvents for extraction of functional components from plant-based products: a promising approach. Sustain Chem. Pharm. 33, 101102. https://doi.org/10.1016/j.scp.2023.101102.

Bergua, F., Castro, M., Lafuente, C., Artal, M., 2022a. Thymol+l-menthol eutectic mixtures: Thermophysical properties and possible applications as decontaminants. J. Mol. Liq. 368, 120789. https://doi.org/10.1016/j.molliq.2022.120789.

Bergua, F., Castro, M., Muñoz-Embid, J., Lafuente, C., Artal, M., 2021. Hydrophobic eutectic solvents: thermophysical study and application in removal of pharmaceutical products from water. Chem. Eng. J. 411. https://doi.org/10.1016/j.cej.2021.128472.

Bergua, F., Castro, M., Muñoz-Embid, J., Lafuente, C., Artal, M., 2022b. L-menthol-based eutectic solvents: characterization and application in the removal of drugs from water. J. Mol. Liq. 352, 118754. https://doi.org/10.1016/j.molliq.2022.118754.

Boateng, I.D., 2023. Evaluating the status quo of deep eutectic solvent in food chemistry. Potentials and limitations. Food Chem. https://doi.org/10.1016/j.foodchem.2022.135079.

Case, I.-S.D.A., Brozell, S., Cerutti, D., Cheatham, T., Cruzeiro, V., Darden, T., Duke, D.G., R., Gilson, M., Gohlke, H., Goetz, A., Greene, D., Harris, R., Homeyer, N., Izadi, S., Kovalenko, T.A., Lee, T., LeGrand, S., Li, P., Lin, C., Liu, J., Luchko, T., Luo, R., Mermelstein, D., Merz, Y.K., Monard, G., Nguyen, C., Nguyen, H., Omelyan, I., Onufriev, A., Pan, F., Qi, R., Roe, D., Roitberg, C.A., Schott-Verdugo, S., Shen, J., Simmerling, C., Smith, J., Salomon-Ferrer, R., Swails, J., Walker, J.R., Wei, H., Wolf, R., Wu, X., Xiao, L., York, D., Kollman, P., 2018. Amber 2018.

Castro-Muñoz, R., Can Karaça, A., Saeed Kharazmi, M., Boczkaj, G., Hernández-Pinto, F. J., Anusha Siddiqui, S., Jafari, S.M., 2023. Deep eutectic solvents for the food industry: extraction, processing, analysis, and packaging applications–a review. Crit. Rev. Food Sci. Nutr. https://doi.org/10.1080/10408398.2023.2230500.

Charisiadis, P., Kontogianni, V., Tsiafoulis, C., Tzakos, A., Siskos, M., Gerothanassis, I., 2014. 1H NMR as a structural and analytical tool of intra- and intermolecular hydrogen bonds of phenol-containing natural products and model compounds. Molecules 19, 13643–13682. https://doi.org/10.3390/molecules190913643.

Chen, W., Viljoen, A.M., 2010. Geraniol - a review of a commercially important fragrance material. South Afr. J. Bot. 76, 643–651. https://doi.org/10.1016/j.sajb.2010.05.008.

Cherniakova, M., Varchenko, V., Belikov, K., 2023. Menthol-Based (Deep) eutectic solvents: a review on properties and application in extraction. Chem. Rec. https://doi.org/10.1002/tcr.202300267.

Claridge, T., 2016. High-Resolution NMR Techniques in Organic Chemistry. Elsevier. https://doi.org/10.1016/C2015-0-04654-8.

Cotterman, R.L., Prausnitz, J.M., 1986. Molecular thermodynamics for fluids at low and high densities. Part II: Phase equilibria for mixtures containing components with large differences in molecular size or potential energy. AIChE J. 32, 1799–1812.

D'Agostino, C., Harris, R.C., Abbott, A.P., Gladden, L.F., Mantle, M.D., 2011. Molecular motion and ion diffusion in choline chloride based deep eutectic solvents studied by 1H pulsed field gradient NMR spectroscopy. Phys. Chem. Chem. Phys. 13, 21383–21391. https://doi.org/10.1039/C1CP22554E.

Dai, Y., Witkamp, G.-J., Verpoorte, R., Choi, Y.H., 2015. Tailoring properties of natural deep eutectic solvents with water to facilitate their applications. Food Chem. 187, 14–19. https://doi.org/10.1016/j.foodchem.2015.03.123.

Delso, I., Lafuente, C., Muñoz-Embid, J., Artal, M., 2019. NMR study of choline chloride-based deep eutectic solvents. J. Mol. Liq. 290, 111236. https://doi.org/10.1016/j.molliq.2019.111236.

van der Spoel, D., van Maaren, P.J., Larsson, P., Tîmneanu, N., 2006. Thermodynamics of hydrogen bonding in hydrophilic and hydrophobic media. J. Phys. Chem. B 110, 4393–4398. https://doi.org/10.1021/jp0572535.

Devi, M., Moral, R., Thakuria, S., Mitra, A., Paul, S., 2023. Hydrophobic deep eutectic solvents as greener substitutes for conventional extraction media: examples and techniques. ACS Omega 8, 9702–9728. https://doi.org/10.1021/acsomega.2c07684.

Di, J., Li, Q., Ma, C., He, Y.-C., 2023. An efficient and sustainable furfurylamine production from biomass-derived furfural by a robust mutant ω-transaminase biocatalyst. Bioresour. Technol. 369, 128425. https://doi.org/10.1016/j.biortech.2022.128425.

Duarte, A.R.C., Ferreira, A.S.D., Barreiros, S., Cabrita, E., Reis, R.L., Paiva, A., 2017. A comparison between pure active pharmaceutical ingredients and therapeutic deep eutectic solvents: Solubility and permeability studies. Eur. J. Pharm. Biopharm. 114, 296–304. https://doi.org/10.1016/j.ejpb.2017.02.003.

Essmann, U., Perera, L., Berkowitz, M.L., Darden, T., Lee, H., Pedersen, L.G., 1995. A smooth particle mesh Ewald method. J. Chem. Phys. 103, 8577–8593. https://doi.org/10.1063/1.470117.

Falleh, H., Ben Jemaa, M., Saada, M., Ksouri, R., 2020. Essential oils: a promising eco-friendly food preservative. Food Chem. 330, 127268. https://doi.org/10.1016/j.foodchem.2020.127268.

Fan, C., Liu, Y., Sebbah, T., Cao, X., 2021a. A theoretical study on terpene-based natural deep eutectic solvent: relationship between viscosity and hydrogen-bonding interactions. Glob. Chall. 5. https://doi.org/10.1002/gch2.202000103.

Fan, C., Sebbah, T., Liu, Y., Cao, X., 2021b. Terpenoid-capric acid based natural deep eutectic solvent: insight into the nature of low viscosity. Clean. Eng. Technol. 3, 100116. https://doi.org/10.1016/j.clet.2021.100116.

Franklin, 2016. (12) United States Patent (45) Date of Patent: (54) (75) (73) (*) (21) (22) (86) (87) (65) (60) (51) (52) (58) compositions and methods comprising terpenes or terpene mixturesselected from thymol, eugenol, geraniol, citral, and l-carvone.

Fröhlich, H., 1948. General theory of the static dielectric constant. Transactions of. Faraday Soc. 44, 238–243. https://doi.org/10.1039/TF9484400238.

Gabriele, F., Chiarini, M., Germani, R., Tiecco, M., Spreti, N., 2019. Effect of water addition on choline chloride/glycol deep eutectic solvents: characterization of their structural and physicochemical properties. J. Mol. Liq. 291, 111301. https://doi.org/10.1016/j.molliq.2019.111301.

Gao, R., Li, Q., Chai, H., He, Y., Yang, Z., Ma, C., 2023. Synthesis of 5-hydroxymethyl-2-furfurylamine from bread waste via two-step reaction. ACS Sustain Chem. Eng. 11, 15315–15327. https://doi.org/10.1021/acssuschemeng.3c04032.

Ghaedi, H., Ayoub, M., Sufian, S., Shariff, A.M., Lal, B., 2017. The study on temperature dependence of viscosity and surface tension of several Phosphonium-based deep eutectic solvents. J. Mol. Liq. 241, 500–510. https://doi.org/10.1016/j.molliq.2017.06.024.

González-Laredo, R.F., Sayago-Monreal, V.I., Moreno-Jiménez, M.R., Rocha-Guzmán, N. E., Gallegos-Infante, J.A., Landeros-Macías, L.F., Rosales-Castro, M., 2023. Natural deep eutectic solvents (<scp>NaDES</scp>) as an emerging technology for the valorisation of natural products and agro-food residues: a review. Int J. Food Sci. Technol. 58, 6660–6673. https://doi.org/10.1111/ijfs.16641.

Gross, J., Sadowski, G., 2000. Application of perturbation theory to a hard-chain reference fluid: An equation of state for square-well chains. Fluid Phase Equilib. 168, 183–199. https://doi.org/10.1016/S0378-3812(00)00302-2.

Gross, J., Sadowski, G., 2001. Perturbed-chain SAFT: an equation of state based on a perturbation theory for chain molecules. Ind. Eng. Chem. Res 40, 1244–1260. https://doi.org/10.1021/ie0003887.

Guggenheim, E.A., 2004. The principle of corresponding states. J. Chem. Phys. 13, 253–261. https://doi.org/10.1063/1.1724033.

Gutiérrez, A., Atilhan, M., Aparicio, S., 2020. Theoretical Study on Deep Eutectic Solvents as Vehicles for the Delivery of Anesthetics. J. Phys. Chem. B, acs. jpcb.9b11756. https://doi.org/10.1021/acs.jpcb.9b11756.

Gutiérrez-Sánchez, P., Rodríguez-Llorente, D., Navarro, P., Águeda, V.I., Álvarez-Torrellas, S., García, J., Larriba, M., 2022. Extraction of antibiotics identified in the EU Watch List 2020 from hospital wastewater using hydrophobic eutectic solvents and terpenoids. Sep Purif. Technol. 282, 14–16. https://doi.org/10.1016/j.seppur.2021.120117.

Harten, P., Martin, T., Gonzalez, M., Young, D., 2020. The software tool to find greener solvent replacements, PARIS III. Environ. Prog. Sustain Energy 39, 1–7. https://doi.org/10.1002/ep.13331.

Hernández-Serrano, V., Muñoz-Embid, J., Bergua, F., Lafuente, C., Artal, M., 2023. pVT behaviour of hydrophilic and hydrophobic eutectic solvents. J. Mol. Liq. 382. https://doi.org/10.1016/j.molliq.2023.122019.

Hockney, R., 1970. The Potential Calculation and Some Applications. In: Methods in Com-Putational Physics. Academic Press, New York, pp. 135–211.

Humphrey, W., Dalke, A., Schulten, K., 1996. VMD: visual molecular dynamics. J. Mol. Graph 14, 33–38. https://doi.org/10.1016/0263-7855(96)00018-5.

Jacobson, B., 2004. Ultrasonic velocity in liquids and liquid mixtures. J. Chem. Phys. 20, 927–928. https://doi.org/10.1063/1.1700615.

Jasper, J.J., 1972. The surface tension of pure liquid compounds. J. Phys. Chem. Ref. Data 1, 841–1010. https://doi.org/10.1063/1.3253106.

Johnson, E.R., Keinan, S., Mori-Sánchez, P., Contreras-García, J., Cohen, A.J., Yang, W., 2010. Revealing noncovalent interactions. J. Am. Chem. Soc. 132, 6498–6506. https://doi.org/10.1021/ja100936w.

Jones, F.E., Harris, G.L., 1992. ITS-90 density of water formulation for volumetric standards calibration. J. Res Natl. Inst. Stand Technol. 97, 335.

Larrañaga, M.D., Lewis Sr, R.J., Robert, A., 2016. Hawley's condensed chemical dictionary. (No Title).

Laursen, T., 2012. VLXE ApS.

Li, X., Tang, W., He, Y.-C., 2023. Integrated understanding of acidic deep eutectic solvent choline chloride: Oxalic acid pretreatment to enhance the enzymatic hydrolysis of rape straw. Ind. Crops Prod. 206, 117691. https://doi.org/10.1016/j.indcrop.2023.117691.

Linstrom, P.J., Mallard, W.G., 2020. NIST Chemistry Webbok, NIST Standard Reference Database Number 69,. Gaithersburg MD, 20899. https://doi.org/10.18434/T4D303.

Loncharich, R.J., Brooks, B.R., Pastor, R.W., 1992. Langevin dynamics of peptides: the frictional dependence of isomerization rates of *N*-acetylalanyl-*N′*-methylamide. Biopolymers 32, 523–535. https://doi.org/10.1002/bip.360320508.

Luzar, A., Chandler, D., 1993. Structure and hydrogen bond dynamics of water–dimethyl sulfoxide mixtures by computer simulations. J. Chem. Phys. 98, 8160–8173. https://doi.org/10.1063/1.464521.

Malik, A., Kashyap, H.K., 2021. Heterogeneity in hydrophobic deep eutectic solvents: SAXS prepeak and local environments. Phys. Chem. Chem. Phys. 23, 3915–3924. https://doi.org/10.1039/D0CP05407K.

Marchel, M., Cieśliński, H., Boczkaj, G., 2022. Deep eutectic solvents microbial toxicity: current state of art and critical evaluation of testing methods. J. Hazard Mater. 425. https://doi.org/10.1016/j.jhazmat.2021.127963.

Marchel, M., Rayaroth, M.P., Wang, C., Kong, L., Khan, J.A., Boczkaj, G., 2023. Hydrophobic (deep) eutectic solvents (HDESs) as extractants for removal of pollutants from water and wastewater – a review. Chem. Eng. J. 475, 144971. https://doi.org/10.1016/j.cej.2023.144971.

Marchese, A., Orhan, I.E., Daglia, M., Barbieri, R., Di Lorenzo, A., Nabavi, S.F., Gortzi, O., Izadi, M., Nabavi, S.M., 2016. Antibacterial and antifungal activities of thymol: a brief review of the literature. Food Chem. 210, 402–414. https://doi.org/10.1016/j.foodchem.2016.04.111.

Martínez, L., Andrade, R., Birgin, E.G., Martínez, J.M., 2009. P <scp>ACKMOL</scp>: A package for building initial configurations for molecular dynamics simulations. J. Comput. Chem. 30, 2157–2164. https://doi.org/10.1002/jcc.21224.

Martins, M.A.R., Carvalho, P.J., Palma, A.M., Domańska, U., Coutinho, J.A.P., Pinho, S. P., 2017. Selecting critical properties of terpenes and terpenoids through group-contribution methods and equations of state. Ind. Eng. Chem. Res 56, 9895–9905. https://doi.org/10.1021/acs.iecr.7b02247.

Martins, M.A.R., Crespo, E.A., Pontes, P.V.A., Silva, L.P., Bülow, M., Maximo, G.J., Batista, E.A.C., Held, C., Pinho, S.P., Coutinho, J.A.P., 2018. Tunable hydrophobic eutectic solvents based on terpenes and monocarboxylic acids. ACS Sustain Chem. Eng. 6, 8836–8846. https://doi.org/10.1021/acssuschemeng.8b01203.

Méndez-Morales, T., Carrete, J., Bouzón-Capelo, S., Pérez-Rodríguez, M., Cabeza, Ó., Gallego, L.J., Varela, L.M., 2013. MD simulations of the formation of stable clusters in mixtures of alkaline salts and imidazolium-based ionic liquids. J. Phys. Chem. B 117, 3207–3220. https://doi.org/10.1021/jp312669r.

Panda, D.K., Bhargava, B.L., 2022. Molecular dynamics investigation of non-ionic deep eutectic solvents. J. Mol. Graph Model 113, 108152. https://doi.org/10.1016/j.jmgm.2022.108152.

Pelofsky, A.H., 1966. Surface Tension-Viscosity Relation for Liquids. J. Chem. Eng. Data 11, 394–397. https://doi.org/10.1021/je60030a031.

Perumal, A.B., Huang, L., Nambiar, R.B., He, Y., Li, X., Sellamuthu, P.S., 2022. Application of essential oils in packaging films for the preservation of fruits and vegetables: a review. Food Chem. 375, 131810. https://doi.org/10.1016/j.foodchem.2021.131810.

Pitacco, W., Samorì, C., Pezzolesi, L., Gori, V., Grillo, A., Tiecco, M., Vagnoni, M., Galletti, P., 2022. Extraction of astaxanthin from Haematococcus pluvialis with hydrophobic deep eutectic solvents based on oleic acid. Food Chem. 379. https://doi.org/10.1016/j.foodchem.2022.132156.

Posada, E., Roldán-Ruiz, M.J., Jiménez Riobóo, R.J., Gutiérrez, M.C., Ferrer, M.L., del Monte, F., 2019. Nanophase separation in aqueous dilutions of a ternary DES as revealed by Brillouin and NMR spectroscopy. J. Mol. Liq. 276, 196–203. https://doi.org/10.1016/j.molliq.2018.11.139.

Program, N.T., n.d. Institute of Environmental Health Sciences, National Institutes of Health (NTP). 1992. National Toxicology Program Chemical Repository Database. Research Triangle Park, North Carolina.

Rodríguez-Llorente, D., Bengoa, A., Pascual-Muñoz, G., Navarro, P., Águeda, V.I., Delgado, J.A., Álvarez-Torrellas, S., García, J., Larriba, M., 2019. Sustainable recovery of volatile fatty acids from aqueous solutions using terpenoids and eutectic solvents. ACS Sustain Chem. Eng. 7, 16786–16794. https://doi.org/10.1021/acssuschemeng.9b04290.

Rodríguez-Llorente, D., Cañada-Barcala, A., Muñoz, C., Pascual-Muñoz, G., Navarro, P., Santiago, R., Águeda, V.I., Álvarez-Torrellas, S., García, J., Larriba, M., 2020. Separation of phenols from aqueous streams using terpenoids and hydrophobic eutectic solvents. Sep Purif. Technol. 251, 117379. https://doi.org/10.1016/j.seppur.2020.117379.

Rodríguez-Llorente, D., Navarro, P., Santiago, R., Águeda, V.I., Álvarez-Torrellas, S., García, J., Larriba, M., 2021. Extractive removal and recovery of bisphenol A from aqueous solutions using terpenoids and hydrophobic eutectic solvents. J. Environ. Chem. Eng. 9. https://doi.org/10.1016/j.jece.2021.106128.

Roe, D.R., Cheatham, T.E., 2013. PTRAJ and CPPTRAJ: Software for Processing and Analysis of Molecular Dynamics Trajectory Data. J. Chem. Theory Comput. 9, 3084–3095. https://doi.org/10.1021/ct400341p.

Schaeffer, N., Abranches, D.O., Silva, L.P., Martins, M.A.R., Carvalho, P.J., Russina, O., Triolo, A., Paccou, L., Guinet, Y., Hedoux, A., Coutinho, J.A.P., 2021. Non-ideality in thymol + menthol type v deep eutectic solvents. ACS Sustain. Chem. Eng. 9, 2203–2211. https://doi.org/10.1021/acssuschemeng.0c07874.

Schafer, N., Balwierz, R., Biernat, P., Ochędzan-Siodłak, W., Lipok, J., 2023. Natural Ingredients of Transdermal Drug Delivery Systems as Permeation Enhancers of Active Substances through the *Stratum Corneum*. Mol. Pharm. 20, 3278–3297. https://doi.org/10.1021/acs.molpharmaceut.3c00126.

Scientific Opinion on the safety and efficacy of phenol derivatives containing ring-alkyl, ring-alkoxy and side-chains with an oxygenated functional group (chemical group 25) when used as flavourings for all species, 2012. EFSA Journal 10. https://doi.org/10.2903/j.efsa.2012.2573.

Sels, H., De Smet, H., Geuens, J., 2020. SUSSOL-Using artificial intelligence for greener solvent selection and substitution. Molecules 25, 1–26. https://doi.org/10.3390/molecules25133037.

Shamshina, J.L., Rogers, R.D., 2023. Ionic liquids: new forms of active pharmaceutical ingredients with unique, tunable properties. Chem. Rev. 123, 11894–11953. https://doi.org/10.1021/acs.chemrev.3c00384.

Sportiello, L., Favati, F., Condelli, N., Di Cairano, M., Caruso, M.C., Simonato, B., Tolve, R., Galgano, F., 2023. Hydrophobic deep eutectic solvents in the food sector: Focus on their use for the extraction of bioactive compounds. Food Chem. https://doi.org/10.1016/j.foodchem.2022.134703.

Štejfa, V., Dergal, F., Mokbel, I., Fulem, M., Jose, J., Růžička, K., 2015. Vapor pressures and thermophysical properties of selected monoterpenoids. Fluid Phase Equilib. 406, 124–133. https://doi.org/10.1016/j.fluid.2015.07.031.

Tang, Z., Fan, B., Tang, W., He, Y.-C., Ma, C., 2024. Comprehensive understanding of co-producing fermentable sugar, furfural, and xylo-oligosaccharides through the pretreatment with CTAB-based deep eutectic solvent containing Brønsted A and Lewis acid. Chem. Eng. J. 488, 150637. https://doi.org/10.1016/j.cej.2024.150637.

The State of Food Security and Nutrition in the World 2022, 2022. FAO. https://doi.org/10.4060/cc0639en.

Van Osch, D.J.G.P., Dietz, C.H.J.T., Van Spronsen, J., Kroon, M.C., Gallucci, F., Van Sint Annaland, M., Tuinier, R., 2019. A search for natural hydrophobic deep eutectic solvents based on natural components. ACS Sustain Chem. Eng. 7, 2933–2942. https://doi.org/10.1021/acssuschemeng.8b03520.

Velez, C., Acevedo, O., 2022. Simulation of deep eutectic solvents: progress to promises. WIREs Comput. Mol. Sci. 12. https://doi.org/10.1002/wcms.1598.

Walker, P.J., Yew, H.-W., Riedemann, A., 2022. Clapeyron.jl: an extensible, open-source fluid thermodynamics toolkit. Ind. Eng. Chem. Res 61, 7130–7153. https://doi.org/10.1021/acs.iecr.2c00326.

Wang, J., Wolf, R.M., Caldwell, J.W., Kollman, P.A., Case, D.A., 2004. Development and testing of a general amber force field. J. Comput. Chem. 25, 1157–1174. https://doi.org/10.1002/jcc.20035.

Wu, B., Yamashita, Y., Endo, T., Takahashi, K., Castner, E.W., 2016. Structure and dynamics of ionic liquids: Trimethylsilylpropyl-substituted cations and bis(sulfonyl) amide anions. J. Chem. Phys. 145. https://doi.org/10.1063/1.4972410.